

Multipath Exploitation for Enhanced Defect Imaging Using Lamb Waves

Andrew Golato¹, Fauzia Ahmad², Sridhar Santhanam³, and Moeness G. Amin⁴

***Abstract*—This paper presents a multipath exploitation approach for defect imaging in thin-walled structures using Lamb waves under the sparse reconstruction framework. An image of the defects in the region of interest is obtained by inverting a multipath propagation model via group sparse reconstruction. This permits accurate imaging of regions close to the structure boundary without the introduction of ‘false’ defects or ghosts. Real-data measurements of defects close to the edge of an aluminum plate are used to demonstrate the effectiveness of the multipath exploitation scheme.**

***Index Terms*—Sparse reconstruction, Lamb waves, multipath exploitation, structural health monitoring.**

I. INTRODUCTION

Use of Lamb waves is emerging as a primary means for the assessment of the integrity of thin-walled structures [1-4]. Lamb waves are the unique solutions to the elastic wave equation for a thin plate with traction free surface conditions [5]. These solutions are multimodal in nature, with the modes being separated into sets of symmetric (S) and anti-symmetric (A) modes. The number of distinct propagating modes in a given structure is a function of the plate thickness and the excitation frequency. Transducer size also affects the relative strength of the individual modes. As such, the propagating wave can be reduced to a single dominant (A or S) mode by an appropriate

choice of the transducer and the excitation frequency [6].

A number of approaches have been developed for imaging defects in thin-walled structures using guided Lamb waves generated by arrays of ultrasonic piezoelectric transducers [7]. An efficient technique is the use of an array of ultrasonic transducers that generate and receive guided waves in a pitch-catch configuration. Signals received by the transducers in the array can be processed with appropriate algorithms to reveal the presence of defects. Among these, the delay and sum algorithm is simple to implement, though it is prone to imaging errors [8]. Tomographical methods have been developed as well, but these techniques require a dense array of transducers [7]. Sparse reconstruction methods have emerged recently as viable techniques to image defects using a sparse array of transducers [9, 10]. For a small number of defects, these methods have been shown to be robust in reconstructing the images of defects in the structure.

When interrogating a structure such as a plate with single-mode Lamb waves, the received signals not only contain the direct scatterings from the structural defects, but also the secondary reflections arising due to wave interactions with the defect and plate boundaries. These multipath reflections have typically been avoided by restricting the region of interest (ROI) to only the interior regions of the plate under examination [8-11]. However, this hinders the localization of defects in regions close to the structure boundaries. Some recent work using data-driven model-based approaches has shown robustness in examining regions in the presence of accounted-for and unaccounted-for interference from edge reflections [12, 13]. However, these authors have not attempted to exploit the additional information provided by edge reflections. To address this issue, we propose a Lamb wave based sparse reconstruction method to exploit the defect information in multipath reflections to provide enhanced localization capability in regions close to the structure edges.

Multipath contributions have been utilized in the recent past for defect imaging in nondestructive evaluation (NDE) and Structural Health Monitoring (SHM) applications [14-17]. In [14], the authors exploited the multipath returns in delay-and-sum beamforming to reveal shadowed parts of the defects, thereby enabling defect perimeter detection in ultrasonic NDE. In [15], the authors proposed a multipath guided wave imaging method, which generates an enhanced image of the ROI by comparing, via deconvolution, the received signals with a database of scattered signal estimates. The latter were obtained from wavefield data collected with a scanning laser vibrometer. Time-reversal methods were applied in [16] to exploit multipath propagation in SHM. In [17], multiple ultrasonic echoes caused by reflections from the plate's boundaries are considered and an analytical model is proposed to estimate the envelope of scattered waves. Correlation between the estimated and experimental data is used to generate images. However, the aforementioned methods do not utilize the sparsity property of the defects in an otherwise pristine structure for image reconstruction. This provides the motivation for our work which exploits multipath propagation to enhance defect imaging within the sparse reconstruction framework.

This paper focuses on the formulation and experimental validation of a sparsity-based multipath exploitation scheme. It significantly extends previous preliminary work by the authors [18] which presented results based on simulations. Our scheme is based on a signal model that considers several multipath signals in addition to the direct path signal. The fundamental anti-symmetric mode (A_0) is utilized to collect real-data measurements from an aluminum plate with one and two symmetric defects. Using the group sparsity constraint, image reconstruction is performed jointly across all signal contributions.

The remainder of the paper is organized as follows. In Section II, we present the signal model and the group sparse reconstruction framework for the sparsity-based multipath exploitation

approach. Section III describes the experimental setup and presents the reconstruction results. Section IV contains the concluding remarks.

II. SIGNAL MODEL

Assume a network of M piezoelectric transducers attached to the surface of a thin plate and operated in pitch-catch mode. These M transducers provide $L = M(M - 1)/2$ unique transmitter-receiver combinations. Let the transmitter and receiver locations corresponding to the l th pair be denoted by \mathbf{t}_l and \mathbf{r}_l , respectively. Assume the excited waveform, $h(t)$, is a windowed sinusoidal signal, whose frequency is selected to provide a single dominant A_0 mode. Access to baseline signals collected with no defect present is assumed [9, 10] and Optimal Baseline Subtraction is employed to minimize temperature-dependent baseline mismatch [19].

Consider P defects present in the plate with the p th defect located at \mathbf{s}_p . Let the ROI be divided into $N \gg P$ pixels. For each transmitter-defect-receiver combination, there exists a number of scattering paths due to the structural edge multipath phenomenon. For illustration, we consider the scenario depicted in Fig. 1(a) and 1(b), where one direct scatter path, two first-order multipath (involving single interaction with the boundary), and one second-order multipath (also referred to as the “W” path involving boundary reflection before and after interaction with the defect) exist between the transmitter and the receiver via the p th defect. The baseline-subtracted received signal, $z_l(t)$, corresponding to the l th transmitter-receiver pair, can be written as

$$z_l(t) = \sum_{p=0}^{P-1} [g_{lp}^0(t) + g_{lp}^1(t) + g_{lp}^2(t) + g_{lp}^3(t)], \quad (1)$$

where $\{g_{lp}^m(t), m=0,1,2,3\}$ are direct and multipath defect scattered waves. These signals can be expressed utilizing their respective Fourier transforms as

$$G_{lp}^0 = x_{p,0}H(f) \exp\left(\frac{j2\pi f(\|t_l - s_p\|_2 + \|r_l - s_p\|_2)}{c_{A_0}(f)}\right) \quad (2)$$

$$G_{lp}^1 = x_{p,1}H(f) \exp\left(\frac{j2\pi f(\|t'_l - s_p\|_2 + \|r_l - s_p\|_2)}{c_{A_0}(f)}\right) \quad (3)$$

$$G_{lp}^2 = x_{p,2}H(f) \exp\left(\frac{j2\pi f(\|t_l - s_p\|_2 + \|r'_l - s_p\|_2)}{c_{A_0}(f)}\right) \quad (4)$$

$$G_{lp}^3 = x_{p,3}H(f) \exp\left(\frac{j2\pi f(\|t'_l - s_p\|_2 + \|r'_l - s_p\|_2)}{c_{A_0}(f)}\right) \quad (5)$$

where $H(f)$ is the Fourier transform of $h(t)$, s_p is the position vector of the p th defect, $c_{A_0}(f)$ is the frequency-dependent phase speed of the A_0 mode, $\|\cdot\|_2$ denotes the l_2 -norm (square root of the sum of the vector square magnitudes), and $\{x_{p,m}, m=0,1,2,3\}$ are the respective defect reflectivities corresponding to the direct and multipath scatterings. The defect reflectivities are assumed to be independent of both frequency and aspect angle. It is noted that variations in defect scattering across the transducer pairs can be readily incorporated by using a block diagonal structure for the dictionary, as detailed in [10]. t'_l and r'_l represent locations of the l th virtual transmitter-receiver pair. The virtual transducers are obtained by reflecting the multipath about the structure boundary, as depicted in Fig. 1(c). This alternate virtual geometry is simply employed to ease the computation of the propagation delays associated with multipath scatters [20]. For

illustration, consider the first-order multipath depicted in Fig. 1(c) between the transmitter at \mathbf{t}_l and receiver at \mathbf{r}_l via the defect at \mathbf{s}_p . The propagation delay associated with this path is identical to that of the path from the virtual transmitter at \mathbf{t}'_l to the defect at \mathbf{s}_p and then on to the receiver at \mathbf{r}_l (also depicted in Fig. 1(c)). Such alternate virtual geometry can be determined for any multipath involving reflections at an edge.

Let \mathbf{z}_l be the $K \times 1$ vector obtained by sampling $z_l(t)$ at time instants, t_k , $k = 0, 1, \dots, K - 1$. Let \mathbf{x}_m , $m = 0, 1, 2, 3$, represent the $N \times 1$ image or scene reflectivity vector corresponding to the m th propagation path. Note that only P entries corresponding to the defect locations are nonzero in each image vector. A linear relationship can be established between the l th signal vector and the image vectors using equations (1) through (5). This relationship can be expressed as [18]

$$\mathbf{z}_l = \Psi_{l,0}\mathbf{x}_0 + \Psi_{l,1}\mathbf{x}_1 + \Psi_{l,2}\mathbf{x}_2 + \Psi_{l,3}\mathbf{x}_3. \quad (6)$$

Here, the (k, n) th elements of the $K \times N$ dictionary matrices $\Psi_{l,0}$, $\Psi_{l,1}$, $\Psi_{l,2}$, and $\Psi_{l,3}$ are, respectively, given by

$$[\Psi_{l,0}]_{k,n} = \mathcal{F}^{-1} \left\{ H(f) \exp \left(\frac{j2\pi f (\|\mathbf{t}_l - \mathbf{s}_n\|_2 + \|\mathbf{r}_l - \mathbf{s}_n\|_2)}{c_{A_0}(f)} \right) \right\} \Big|_{t=t_k} \quad (7)$$

$$[\Psi_{l,1}]_{k,n} = \mathcal{F}^{-1} \left\{ H(f) \exp \left(\frac{j2\pi f (\|\mathbf{t}'_l - \mathbf{s}_n\|_2 + \|\mathbf{r}_l - \mathbf{s}_n\|_2)}{c_{A_0}(f)} \right) \right\} \Big|_{t=t_k} \quad (8)$$

$$[\Psi_{l,2}]_{k,n} = \mathcal{F}^{-1} \left\{ H(f) \exp \left(\frac{j2\pi f (\|\mathbf{t}_l - \mathbf{s}_n\|_2 + \|\mathbf{r}'_l - \mathbf{s}_n\|_2)}{c_{A_0}(f)} \right) \right\} \Big|_{t=t_k}. \quad (9)$$

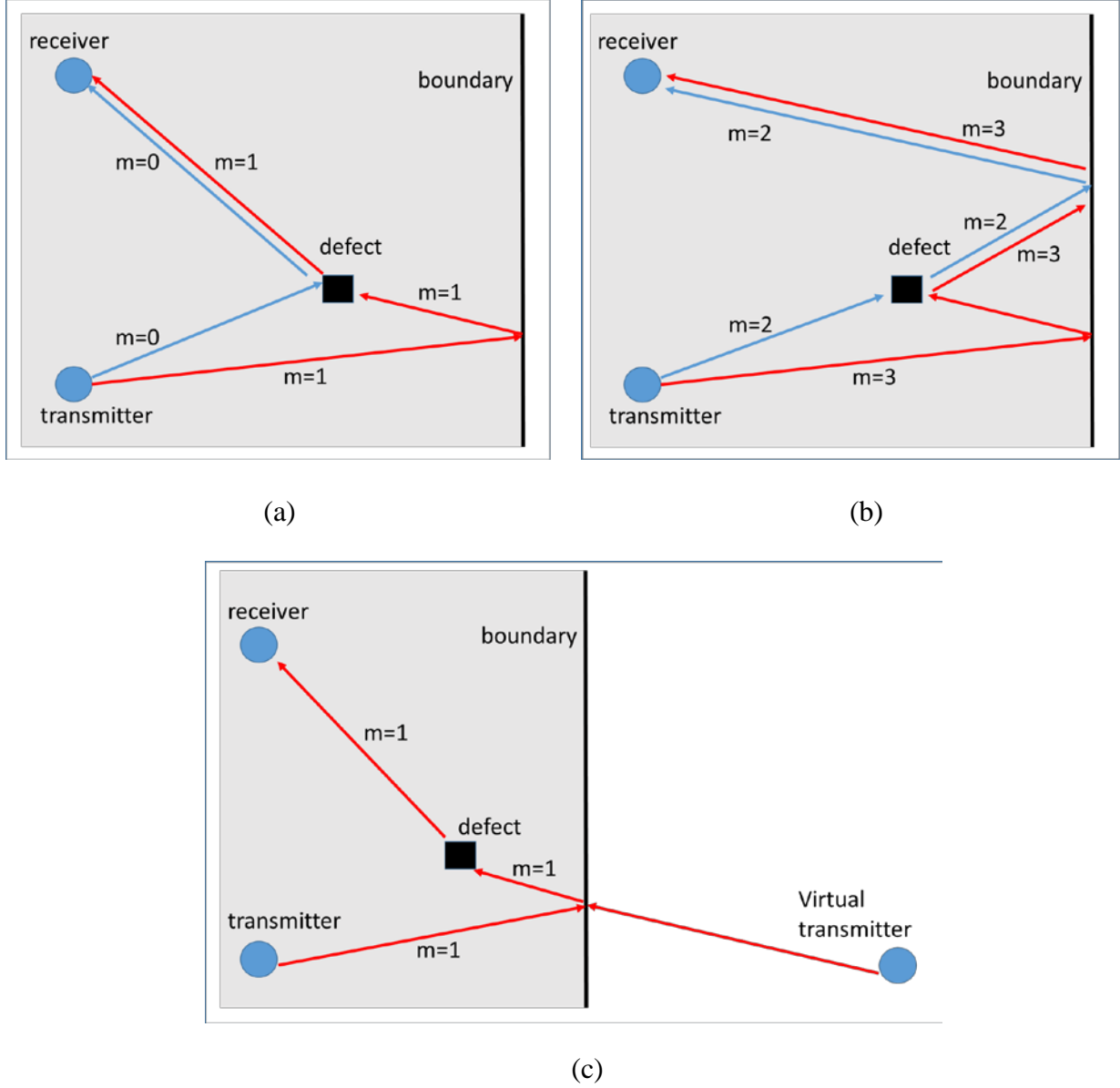


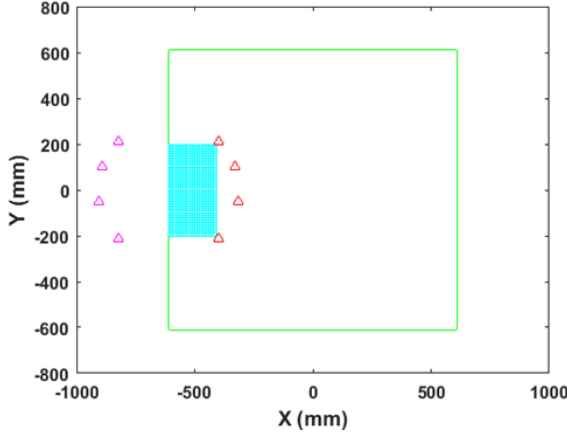
Fig. 1. Schematic showing multiple pathways for waves to travel from a transmitter to a receiver after being scattered by a defect and the plate boundary: (a) the direct scatter path ($m = 0$) and a first-order multipath ($m = 1$); (b) a first order multipath ($m=2$) and a second-order “W” path ($m = 3$); (c) virtual transmitter model; the case of the virtual receiver is constructed analogously. Shaded region represents region of plate.

$$[\Psi_{l,3}]_{k,n} = \mathcal{F}^{-1} \left\{ H(f) \exp \left(\frac{j2\pi f (\|t'_l - s_n\|_2 + \|r'_l - s_n\|_2)}{c_{A_0}(f)} \right) \right\} \Big|_{t=t_k} \quad (10)$$

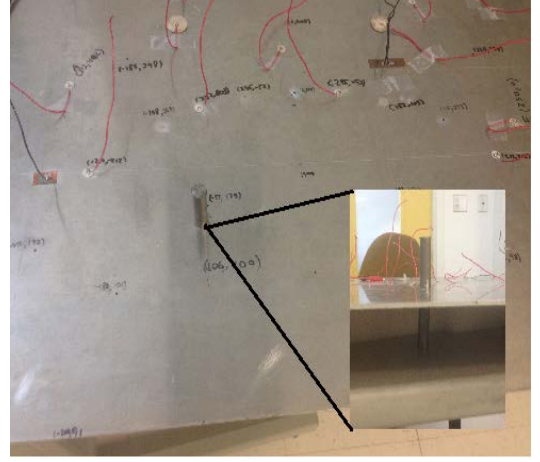
where \mathcal{F}^{-1} denotes the inverse Fourier transform and \mathbf{s}_n is the location of the n th pixel.

Stacking the received signal vectors $\{\mathbf{z}_l, l = 0, 1, \dots, L-1\}$, we obtain the $KL \times 1$ vector $\mathbf{z} = [\mathbf{z}_0^T \ \mathbf{z}_1^T \ \dots \ \mathbf{z}_{L-1}^T]^T$ as

$$\mathbf{z} = \Psi_0 \mathbf{x}_0 + \Psi_1 \mathbf{x}_1 + \Psi_2 \mathbf{x}_2 + \Psi_3 \mathbf{x}_3, \quad (11)$$



(a)



(b)

Fig. 2. (a) Schematic of the layout for experiments 1 through 5. The transducer locations are indicated by red triangles. The corresponding virtual transducer locations are shown as magenta triangles. The imaged region is represented by the dense cyan grid, while the green rectangle represents the physical plate boundaries; (b) Actual experimental setup with the inset showing the symmetric defect (steel rods glued to the top and bottom surfaces).

where the superscript ‘ T ’ denotes matrix transpose and the matrix Ψ_q of size $KL \times N$ is given by

$$\Psi_q = [\Psi_{0,q}^T \ \Psi_{1,q}^T \ \dots \ \Psi_{L-1,q}^T]^T, \text{ for } q = 0, 1, 2, 3. \quad (12)$$

Note that the model does not require the multipath signals to be resolvable. Further, although only first-order and one second-order multipath are considered herein, higher-order multipath involving multiple boundary interactions can be readily incorporated into the signal model. These are ignored in this work because of higher attenuation due to longer associated propagation path

lengths, thereby rendering the arriving wave packets to be of negligible amplitudes [20]. Further, we have only considered a single propagating mode in the signal model. However, in a similar manner to incorporating additional multipath, one could expand the signal model to the multimodal case by creating additional dictionary matrices for various paths under another mode, as dictated by the unique phase velocity curve for that mode. Lastly, additional structural complexities, such as stiffeners, which would also produce multipath, can be readily accounted for and exploited in the signal model.

Since the direct and multipath scatterings describe the same underlying scene, the image vectors \mathbf{x}_0 , \mathbf{x}_1 , \mathbf{x}_2 , and \mathbf{x}_3 exhibit a group sparse structure, where the individual groups extend across the four paths for each pixel location. It should be noted that group sparsity does not refer to the physical span of the defects. To be specific, group sparsity here implies that each modeled multipath dictionary examines the same physical scene. Therefore, if a particular pixel location is assigned a nonzero value (implying a defect is present) in one image vector, the same location must also be assigned a nonzero value in all the other image vectors, since every image vector is capturing the same physical space. As such, group sparse reconstruction can be employed to recover \mathbf{x}_0 , \mathbf{x}_1 , \mathbf{x}_2 , and \mathbf{x}_3 from the measurements \mathbf{z} . This amounts to either solving the problem [21, 22]

$$\hat{\mathbf{x}} = \arg \min_{\mathbf{x}} \frac{1}{2} \|\mathbf{z} - \Psi \mathbf{x}\|_2^2 + \lambda \|\mathbf{x}\|_{2,1}, \quad (13)$$

where $\Psi = [\Psi_0 \ \Psi_1 \ \Psi_2 \ \Psi_3]$, $\mathbf{x} = [\mathbf{x}_0^T \ \mathbf{x}_1^T \ \mathbf{x}_2^T \ \mathbf{x}_3^T]^T$,

and $\|\mathbf{x}\|_{2,1} = \sum_{n=0}^{N-1} \|[x_{n,0} \ x_{n,1} \ x_{n,2} \ x_{n,3}]^T\|_2$, $x_{n,q}$ is the n th element of the q th image

\mathbf{x}_q , $q = 0,1,2,3$, and λ is a regularization parameter, or recovering the group sparse vector \mathbf{x}

through the use of greedy algorithms [23, 24]. In this work, we choose to use a greedy algorithm,

namely, the block version of Orthogonal Matching Pursuit (OMP) for its exceptional efficiency in providing accurate reconstructions in CPU time on the order of 2-3 seconds [24]. Once the recovered vector $\hat{\mathbf{x}}$ has been obtained using the chosen algorithm, a single composite scene representation $\tilde{\mathbf{x}}$ can be obtained as [18]:

$$[\tilde{\mathbf{x}}]_n = \tilde{x}_n = \left\| [\hat{x}_{n,0} \quad \hat{x}_{n,1} \quad \hat{x}_{n,2} \quad \hat{x}_{n,3}]^T \right\|_2 \quad (14)$$

III. EXPERIMENTAL RESULTS

A. Setup and Reconstruction Results

Data measurements were performed using a 1220 mm \times 1220 mm aluminum plate with a thickness of 3.125 mm. While the experiments were performed with an isotropic plate, an extension to an anisotropic plate can be made by properly incorporating the corresponding material properties in the wave propagation model of Section II.

Six different experiments were conducted. More specifically, experiments 1-4 and 6 correspond to a single defect positioned at several different locations, while experiment 5 considers a two-defect case. The primary imaged region for experiments 1 through 5 is a 200 mm \times 400 mm rectangle, as shown in Fig. 2(a). The region is divided into a 21 \times 41 grid resulting in 861 pixel locations. For experiment 6, the ROI is shifted to concentrate on the corner of the plate, away from the transducer array as depicted in Fig. 3. This region is a 150 mm \times 150 mm square, and is divided into a 16 \times 16 pixel grid providing 256 pixels.

A 100 kHz 5-cycle Hanning windowed toneburst was used to induce a dominant A_0 wave mode in the plate. The signal was generated using a National Instruments (NI) PXI 5142 Arbitrary Waveform Generator, in conjunction with a Krohn-Hite Model 7500 Amplifier, whose gain was set to 40 dB so as to ensure a strong incident wave. The received data measurements were collected

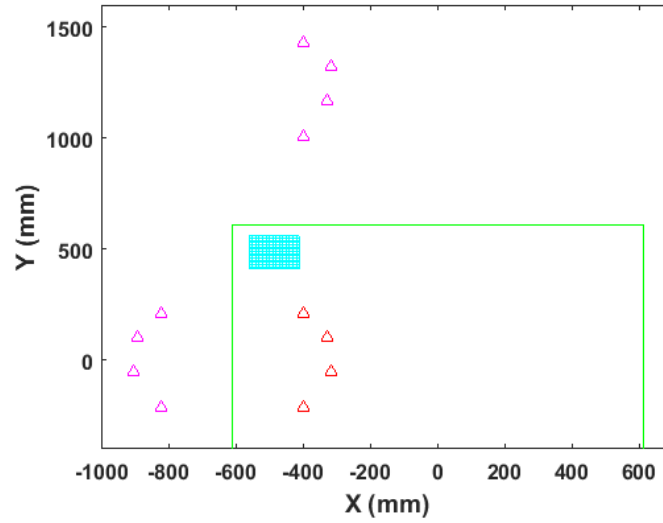


Fig. 3. Schematic of the experimental layout for the corner defect, experiment 6. The actual transducer locations are indicated by red triangles. The imaged region is represented by the dense cyan grid and the green rectangle represents the physical plate boundaries. The magenta triangles located outside the plate represent the locations of the virtual transducers. Note that the bottom of the physical plate has been cut off in the shifted schematic shown here.

via an NI PXI 5105 Digitizer operating at a sampling rate of 1 MHz. The data measurements were averaged over 5000 collections in LabView. Both the PXI 5142 and 5105 were housed in an NI PXI 8108 Embedded Controller. Four Lead Zirconate Titanate piezoelectric transducers were located on a semi-circle of radius 300 mm centered at the midpoint of the left plate boundary, as shown in Fig. 2(a). The transducers are manufactured by APC International, with specifications of 0.22 mm thickness, 10 mm diameter, and polarization such that grounding the plate will ground the bottom surface of the transducer; thereby, a charge flows to the transducer through a wire soldered to the top of the disc. Each defect was introduced by gluing steel rods symmetrically to the top and bottom of the plate, as shown in Fig. 2(b).

Signals were collected for the six distinct transmitter-receiver pairs both in the absence and presence of the defects. Typical signals received from a transmitter receiver pair, in the experimental arrangement of Fig. 2(a), are shown in Fig. 4. Fig. 4(a) shows a baseline signal

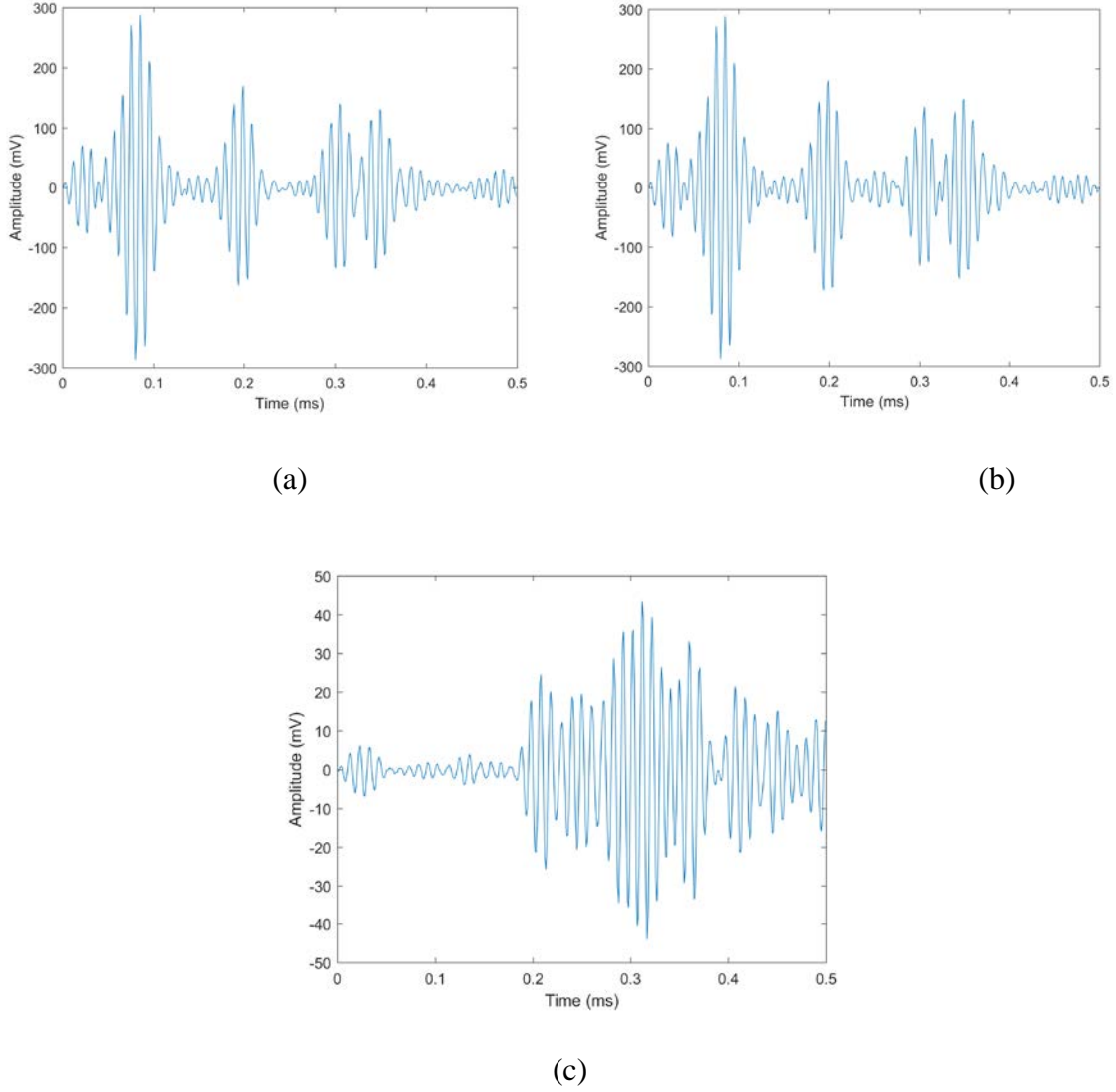


Fig. 4. (a) Baseline signal from a transmitter-receiver pair from the experimental arrangement shown in Fig. 2(a). The baseline signal is collected in the absence of defects. (b) Signal collected from the same transmitter-receiver pair in the presence of a defect. (c) The differenced signal obtained by subtracting the signal in Fig. 4(a) from Fig. 4(b).

obtained in the absence of defects in the ROI. When a defect is present in the ROI, the received signal is altered by the defect as shown in Fig. 4(b). The baseline-subtracted received signal of Fig. 4(c), corresponding to $z_l(t)$ in Eqn. (1), is obtained by subtracting the baseline signal of Fig. 4(a) from the defect-influenced received signal of Fig. 4(b). Differenced signal vectors such as in

Fig. 4(c), obtained from all transmitter-receiver pairs, can be stacked to obtain the experimental signal vector, \mathbf{z} , of Eqn.(11).

TABLE 1
EXPERIMENTAL DEFECT LOCATIONS AND METRIC VALUES

Exp. #	Fig. #	Defect 1 Location (mm)	Defect 2 Location (mm)	NMSE (dB)	SCR (dB)	Distance From nearest selection to true location (mm)
1	4 (a)	(-460, 120)	N/A	2.1932	$-\infty$	140.4
	4 (e)			-2.0873	1.0436	7.0
2	4 (b)	(-560, 100)	N/A	0	$-\infty$	50.0
	4 (f)			-9.9846	4.9923	0.0
3	4 (c)	(-560, -100)	N/A	0.5382	$-\infty$	31.6
	4 (g)			-6.5619	3.2809	0.0
4	4 (d)	(-410, -200)	N/A	0	$-\infty$	210.9
	4 (h)			-6.6891	3.3445	0.0
5	5 (a)	(-540, -100)	(-460, 120)	0	0.6117	64.8
	5 (b)			-9.1393	$+\infty$	0.0
6	6 (a)	(-470, 500)	N/A	0	$-\infty$	51.0
	6 (b)			0	$-\infty$	14.1

Image reconstructions were performed in Matlab utilizing Block OMP (BOMP) for the proposed multipath approach, and OMP for the conventional sparse reconstruction approach, which does not exploit multipath; hence, no group sparsity is employed in the latter. The sparsity estimate for both reconstructions was prescribed as two in all experiments. That is, the sparsity is overdetermined for all experiments except experiment 5. In experiment 5, the reconstruction result corresponds to the case when the sparsity estimate exactly matches the number of defects present in the specimen.

The defect locations for all six experiments and the corresponding associated figure numbers depicting the reconstruction results are provided in Table 1. Figs. 5(a)-5(d) show the reconstruction results for experiments 1-4 using the conventional sparse reconstruction approach which ignores

multipath contributions, while Figs. 5(e)-5(h) depict the results obtained with the proposed group sparse multipath exploitation approach. In all figures, the actual defect location is identified by a black circle. The predicted location(s) of the defect are indicated by colored squares. The left plate boundary and the transducer locations (triangles) are also superimposed on the images. Note that experiments 1-4 correspond to a variety of defect positions within the ROI. More specifically, the defect is located away from the plate edge (Figs. 5(a) and 5(e)), close to the plate edge in the upper half of the ROI (Figs. 5(b) and 5(f)), close to the plate edge in the lower half of the ROI (Fig. 5(c) and 5(g)), and near the corner of the ROI blocking one of the transducers (Fig. 5(d) and 5(h)). We observe from Fig. 5 that the proposed multipath approach was successful in accurately localizing the defect in all considered cases, with the strongest selection assigned to the true target location. In contrast, the conventional approach, which does not account for multipath, failed to properly localize the defect in all instances. These results clearly demonstrate the validity of the proposed approach and show that the proposed approach does not exhibit any bias toward a particular region of the ROI (despite the use of a non-uniformly spaced sparse transducer array). The approach was even successful in the challenging scenario of experiment 4 where some of the transmitter-receiver pairs could not contribute to the reconstruction due to the defect blocking the transducer.

In addition to the qualitative comparison, we employ two metrics, namely, the signal-to-clutter ratio (SCR) and the normalized mean square error (NMSE) to compare the performance of the proposed and conventional approaches. The SCR is defined as the ratio of the maximum intensity of pixels occupying the actual target region (ground truth) to the average intensity of the pixels occupying the clutter region [25]. The clutter region of the image is defined as the area spanned by the physical plate excluding the target region. On the other hand, the NMSE is defined as

$$\text{NMSE} = 10 \log_{10} \left\| \hat{\mathbf{x}}/|\hat{\mathbf{x}}|_{\max} - \mathbf{x}_g/|\mathbf{x}_g|_{\max} \right\|_2^2 \quad (15)$$

where $\mathbf{x}_g/|\mathbf{x}_g|_{\max}$ is the normalized ground truth image. For the scenario at hand, the ground truth image pixel corresponding to the true target location assumes a unit value, while all other pixels are zero. The resultant metric values corresponding to each image in Fig. 5 are presented in Table 1. Note that the conventional approach's inability to provide any localization inside the target region results in a negatively infinite value for the SCR. Further, the NMSE provided in decibels describes a more successful reconstruction by a negative number, thereby implying a small error, whereas non-negative values for the NMSE imply a lack of proper localization inside the target region.

The reconstruction results for the two defect case of experiment 5 are depicted in Fig. 6. The defect locations are specified in Table 1. Again, both defects are properly localized by the proposed multipath approach, as seen in Fig. 6(b), whereas only one of the two defects is accurately localized by the conventional approach, as depicted in Fig. 6(a). The success of the proposed approach and the failure of the conventional approach are also captured in the corresponding values of the aforementioned metrics provided in Table 1. Note that since all of the selections in this case lie within the target region for the multipath approach, the clutter region is empty; therefore, the SCR approaches a positively infinite value.

For experiment 6, which considers a single defect located near the plate corner far from the transducer array, the complexity of the signal model is increased due to the presence of two edges in close proximity of the defect. Nevertheless, the signal model of equation (13) is easily extended via superposition to account for the first- and second-order multipath scatters from the two edges (four paths, as shown in Fig. 1, corresponding to each edge). It should be noted that, in addition to the “W” path associated with each edge, other second-order multipath also exist in consideration

of a two edge interaction whereby the signal scatters off one edge during the transmit path and then off the second edge on the receive path after interaction with the defect and vice versa. These two additional second-order multipath scatters, when included in the signal model, did not provide any reconstruction improvement beyond that achieved with the eight paths involving single-edge based multipath. As such, these are excluded from the remainder of the discussion in this section.

Fig. 7(a) depicts the reconstruction result for experiment 6 when multipath is ignored, whereas Fig. 7(b) shows the image obtained using the proposed multipath exploitation approach. The corresponding values of the SCR and NMSE are listed in Table 1. Compared to the conventional approach which fails to localize the defect, the proposed approach puts the strongest pixel selection in close vicinity of the defect (displaced by 14 mm approximately from the target region in Fig. 7(b)). This localization lies well within the tolerance limit for most engineering applications. The same acceptability, however, does not apply to Fig. 7(a), wherein the displacement of the strongest pixel selection is approximately 51 mm from the target region. Hence, despite a small bias, the proposed approach still outperforms the conventional approach for the challenging case of a defect located near the plate corner far from the transducer array. The biased reconstruction of experiment 6 can be attributed to the significantly higher attenuation for all considered paths due to the longer propagation distances between the defect location and the transducer array, as compared to the scenes considered in experiments 1-4. Improved results can be obtained by choosing transducer locations closer to the plate corner.

B. Performance Analysis

Some discussion is in order with regard to the effects of noisy observations and variations in prescribed scene sparsity on the performance of the proposed multipath exploitation approach. To this end, we first varied the prescribed scene sparsity from 1 to 3 in unit increments and the

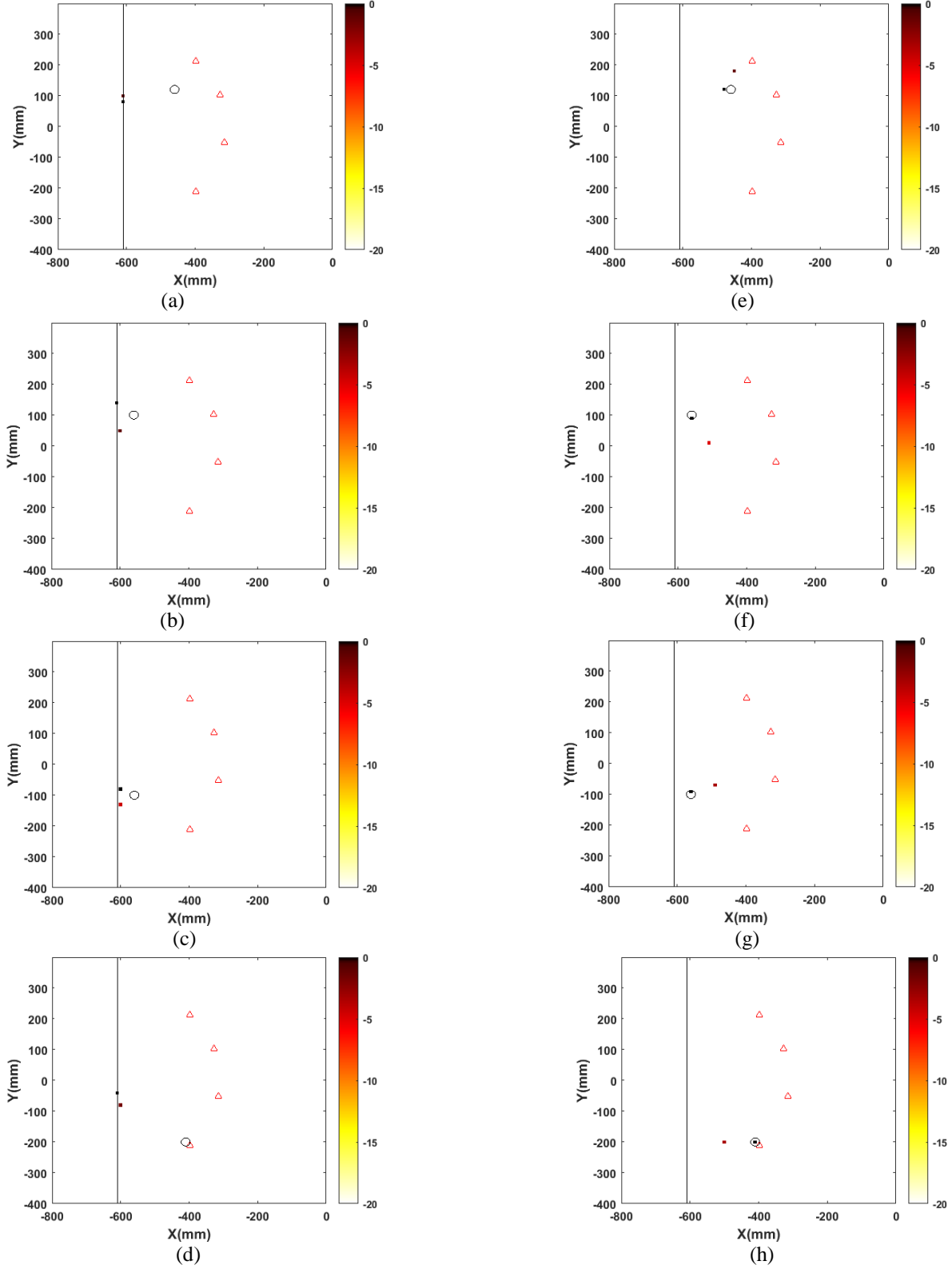


Fig. 5. Reconstructed images for experiments 1 to 4 using (a)-(d) conventional sparse reconstruction not accounting for multipath, and (e)-(h) proposed multipath exploitation approach. The true defect location in each experiment is represented by the black circle. Vertical black line to the left indicates physical plate boundary. The red triangles represent the transducer locations.

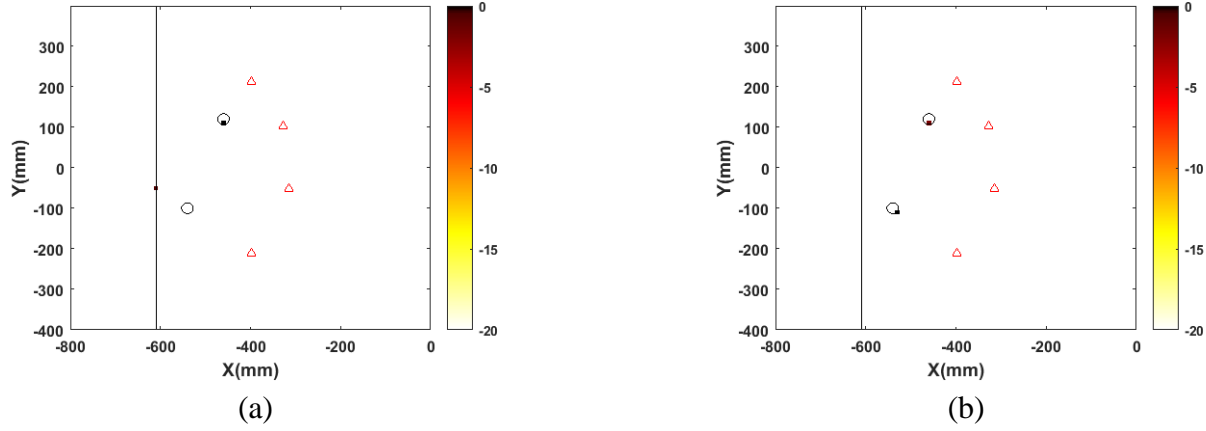


Fig. 6. Reconstruction results for the two defect case using (a) conventional sparse reconstruction, and (b) proposed multipath exploitation approach. The true defect locations are indicated by the black circles. Vertical black line to the left indicates physical boundary of the plate. The red triangles represent the transducer locations.

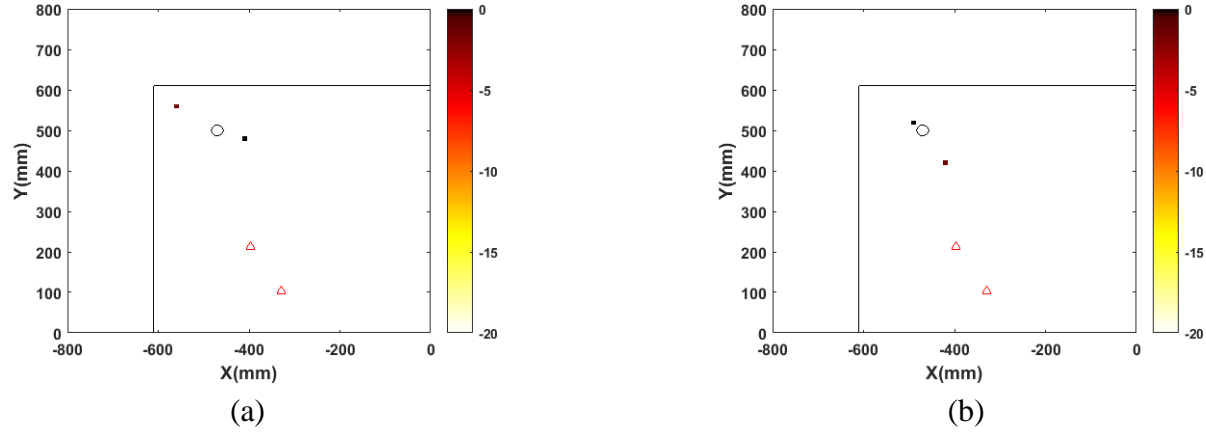


Fig. 7. Reconstructed images for the corner defect case using (a) conventional sparse reconstruction, and (b) proposed multipath exploitation approach. The ROI has been shifted to correspond to the topology depicted in Fig. 3. The true defect location is represented by the circle. Vertical black lines to the left and top of the image indicate physical boundaries of the plate. Note that only two of the transducers are visible in the images.

images corresponding to experiments 1-4 were reconstructed using BOMP for each sparsity value.

The corresponding NMSE and SCR metrics were computed for each reconstructed image and the averaged values across the four different experiments for each specified sparsity are provided in Table 2. As expected, the performance degrades for overdetermined scene sparsity. This is because a higher amount of background noise is reconstructed with increasing number of BOMP iterations.

It is noted that cross validation can be employed to avoid early or late termination of greedy reconstruction algorithms [26].

Next, white Gaussian noise was added to the measurements for experiments 1-4. The signal-to-noise ratio (SNR) was varied from -15 to +20 dB in increments of 5 dB, and the corresponding images were reconstructed using BOMP with a prescribed sparsity of 2. The noise was added to each individual transmitter-receiver pair independently such that the SNR for each pair achieved the desired value. The NMSE and the SCR, averaged over 25 Monte Carlo runs and all four experiments, are plotted vs. SNR in Fig. 8. For SNR values of -5 dB and above, the proposed approach provides, on average, an SCR of 5 dB and NMSE of -10 dB approximately.

TABLE 2
NMSE AND SCR FOR VARYING SPARSITY

Sparsity	NMSE (dB)	SCR (dB)
1	$-\infty$	$+\infty$
2	-6.33	3.55
3	-4.64	3.17

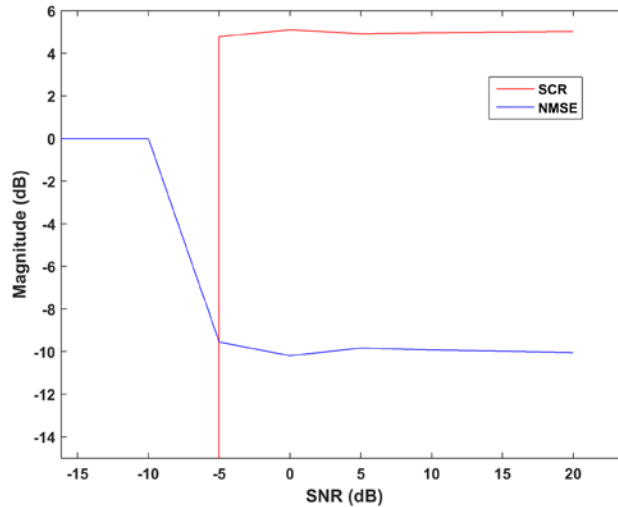


Fig. 8. NMSE and SCR (averaged over 25 Monte Carlo runs and experiments 1-4) vs. SNR.

IV. CONCLUSION

In this paper, we have successfully formulated and experimentally validated a sparsity-based multipath exploitation approach for defect localization in thin-walled plates. Dictionaries, accounting for the associated attenuation and dispersion of Lamb wave propagation, were created for the direct scatter path as well as the first- and second-order (“W”) multipath scatters. The group sparse structure of the image vectors associated with the considered propagation paths was exploited for accurate reconstruction. Both qualitative and quantitative comparisons demonstrated that the multipath exploitation approach significantly outperforms conventional sparse image reconstruction which ignores multipath. Qualitatively, the proposed approach exhibits sufficient robustness to consistently provide accurate reconstruction results. Quantitatively, the considered metrics objectively testify to the accuracy and superiority of the proposed approach.

It is important to note that the proposed approach can be easily modified to account for complexities such as anisotropic plates, the presence of stiffeners, or thickness variations. These complexities and their associated effect on propagations physics can be incorporated into the signal model which produces the dictionary matrix and therefore dictates the reconstruction. By accounting for such complexities, the proposed approach can be used to inspect more complex scenes than the one considered herein.

REFERENCES

- [1] A. Raghavan and C.E.S. Cesnik, “A review of guided wave structural health monitoring,” *Shock and Vibrations Digest*, vol. 39, no. 2, pp. 91-114, 2007.
- [2] S. Santhanam, and R. Demirli, "Reflection and transmission of fundamental Lamb wave modes obliquely incident on a crack in a plate," *Proc. IEEE Int. Ultrasonics Symp.*, pp. 2690-2693, 2012.

- [3] T. Di Ianni, L. De Marchi, A. Perelli, and A. Marzani, “Compressive sensing of full wave field data for structural health monitoring applications,” *IEEE Trans. Ultrason. Ferroelect., Freq. Control* vol. 62, no. 7, pp. 1373-1383, 2015.
- [4] T. Clarke, P. Cawley, P.D. Wilcox, and A.J. Croxford, “Evaluation of the damage detection capability of a sparse-array guided-wave SHM system applied to a complex structure under varying thermal conditions,” *IEEE Trans. Ultrason. Ferroelect., Freq. Control* vol. 56, no. 12, pp. 2666-2678, 2009.
- [5] J. Achenbach, *Wave Propagation in Elastic Solids*, North Holland, New York, 1984.
- [6] V. Giurgiutiu, “Tuned Lamb wave excitation and detection with piezoelectric wafer active sensors for structural health monitoring,” *J. Intel. Mat. Syst. Str.* Vol. 16, no. 4, pp. 291-305, 2005.
- [7] Z. Su and L. Ye, *Identification of Damage using Lamb Waves*, Springer-Verlag, Berlin, 2009.
- [8] C . H. Wang, J. T. Rose, and F. K. Chang, “A synthetic time-reversal imaging method for structural health monitoring,” *Smart Mater.Struct.*, vol. 13, no. 2, pp. 415–423, Apr. 2004
- [9] R.M. Levine, and J.E. Michaels, "Model-based imaging of damage with Lamb waves via sparse reconstruction," *J. Acoust. Soc. Am.* vol. 133, no. 3, pp. 1525-1534, 2013.
- [10] A. Golato, S. Santhanam, F. Ahmad, and M.G. Amin, "Multimodal sparse reconstruction in guided wave imaging of defects in plates", *J. of Electronic Imaging*, 25(4), 2016.
- [11] R.M. Levine, and J.E. Michaels, “Block-Sparse reconstruction and imaging for Lamb wave structural health monitoring,” *IEEE Trans. Ultrason. Ferroelect., Freq. Control* vol. 61, no. 6, pp. 1006-1015, 2014.
- [12] J. Harley, and J. Moura, “Data-driven matched field processing for Lamb wave based structural health monitoring,” *J. Acoust. Soc. Am.* vol.135, no.3, pp.1231-1244, 2014.

- [13]A Perelli, A, et al., "Model-based compressive sensing for damage localization in Lamb wave inspection," *IEEE Trans. Ultrason. Ferroelect., Freq. Control* vol. 60, no. 10, pp. 2089-2097, 2013.
- [14]Y.D. Zhang, X. Shen, R. Demirli, and M.G. Amin, "Ultrasonic flaw imaging via multipath exploitation," *Advances in Acoustics and Vibration*, vol. 2012, Article ID 874081, pp. 1-12, April 2012.
- [15]J.S. Hall and J.E. Michaels, "Multipath ultrasonic guided wave imaging in complex structures," *Structural Health Monitoring*. vol. 14, pp. 345-358, 2015.
- [16]E. Chan, L.R.F. Rose, and C.H. Wang, "Multifrequency approach to imaging damage in stiffened structures exhibiting multi-path reflections," in *Proc. Int. Workshop on Structural Health Monitoring*, Stanford, CA, 2015.
- [17]A. Ebrahimkhanlou, B. Dubuc and S. Salamone, "Damage localization in metallic plate structures using edge-reflected lamb waves," *Smart Mater. Struct.*, vol. 25, Article ID 085035, pp. 1-13, 2016.
- [18]A. Golato, S. Santhanam, F. Ahmad, M.G. Amin, "Multipath exploitation in a sparse reconstruction approach to Lamb wave based structural health monitoring," in *Proc. Int. Workshop on Structural Health Monitoring*, Stanford, CA, 2015.
- [19] A. Croxford, P. Wilcox, G. Konstantinidis and B. Drinkwater, "Strategies for overcoming the effect of temperature on guided wave structural health monitoring," *Proc. SPIE 6532, Health Monitoring of Structural and Biological Systems*, vol. 6532, p. 65321T, 2007.
- [20]M. Leigsnering, F. Ahmad, M.G. Amin, and A. Zoubir, "Multipath exploitation in through-the-wall radar imaging using sparse reconstruction," *IEEE Trans. Aerosp. Electronic Syst.*, vol. 50, no 2, pp. 920-939, 2014.

- [21]W. Deng, W. Yin, and Y. Zhang, “Group sparse optimization by alternating direction method,” Department of Computational and Applied Mathematics, Rice University, Technical Report TR11-06, 2011.
- [22]S.J. Wright, R.D. Nowak, and M.A.T. Figueiredo, “Sparse reconstruction by separable approximation,” *IEEE Trans. Signal Process.* vol. 57, no 7, pp. 2479-2493, 2009.
- [23]J. A. Tropp, “Greed is good: Algorithmic results for sparse approximation,” *IEEE Trans. Inf. Theory*, vol. 50, no. 10, pp. 2231–2242, October 2004.
- [24]Y.C. Eldar, P. Kuppinger, and H. Bolcskei, "Block-sparse signals: Uncertainty relations and efficient recovery," *IEEE Trans. Signal Process.* Vol. 58, no. 6, pp. 3042–3054, 2010.
- [25]Y.-S. Yoon and M. Amin, “Spatial filtering for wall-clutter mitigation in through-the-wall radar imaging,” *IEEE Trans. Geosci. Remote Sens.*, vol. 47, no. 9, pp. 3192 –3208, Sept. 2009.
- [26]P. Boufounos, M. Duarte, and R Baraniuk, “Sparse signal reconstruction from noisy compressive measurements using cross validation,” in *Proc. IEEE Workshop on Statistical Signal Process.*, Madison, WI, 2007, pp. 299–303.